JGR Space Physics

RESEARCH ARTICLE
10.1029/2025JA034151

Delayed Ionospheric Response to Solar Activity: Influence of Geomagnetic Activity

Rajesh Vaishnav[1], **Christoph Jacobi**[1], **Erik Schmölter**[2], **and Hanna Dühnen**[2]

[1]Leipzig Institute for Meteorology, Leipzig University, Leipzig, Germany, [2]German Aerospace Center, Neustrelitz, Germany

Key Points:

- The variations in thermospheric-ionospheric parameters caused by geomagnetic activity have been examined using Thermosphere-Ionosphere-Electrodynamics General Circulation Model simulations
- The influence of geomagnetic activity on ionospheric delay varies with solar activity
- The seasonal variations in ionospheric delay are related to geomagnetic activity

Correspondence to:

R. Vaishnav,
rajesh_ishwardas.vaishnav@uni-leipzig.de

Citation:

Vaishnav, R., Jacobi, C., Schmölter, E., & Dühnen, H. (2025). Delayed ionospheric response to solar activity: Influence of geomagnetic activity. *Journal of Geophysical Research: Space Physics*, *130*, e2025JA034151. https://doi.org/10.1029/2025JA034151

Received 30 APR 2025
Accepted 11 OCT 2025

Abstract The role of geomagnetic activity in the delayed response of the ionosphere along with the solar influences was investigated through a series of controlled simulations of the National Center for Atmospheric Research Thermosphere-Ionosphere-Electrodynamics General Circulation Model under conditions of moderate geomagnetic storms during varying solar activity. In addition, observed ionospheric total electron content data sets were used to investigate the ionospheric delay and to compare it with the model simulations. The ionospheric delay varies spatially and seasonally depending on the solar and geomagnetic activity conditions. The simulations show a global decrease in ionospheric delay during Northern Hemisphere spring, except at high-latitudes in the Northern Hemisphere under moderate geomagnetic activity. The delay increases in the Western Hemisphere during the winter season. We found that the ionospheric delay during the 27-day solar rotation period changes based on whether geomagnetic activity occurs before or after the peak solar rotation day. This study emphasizes the significance of considering the geomagnetic activity when calculating ionospheric delay.

1. Introduction

The thermosphere and ionosphere exhibit spatiotemporal variations influenced by factors such as lower atmospheric forcing, solar radiation, electrodynamics, solar wind, and geomagnetic activity responsible for photochemistry, transport, and electrodynamics processes (Prölss, 2004; Rishbeth, 1998; Rishbeth et al., 2000; Vaishnav et al., 2019). Geomagnetic storms significantly impact the upper atmosphere in both the neutral thermosphere and ionosphere, affecting communication and navigation systems by altering the F-region composition due to increased magnetosphere energy input (Rishbeth et al., 2000). Energy transfer from high to low-latitudes intensifies during storms due to enhanced Joule heating, auroral precipitation, electric fields, and ionospheric conductivity, as noted in various studies (e.g., Burns et al., 2004; Cai et al., 2021; Fuller-Rowell et al., 1994; Qian et al., 2020; Rishbeth et al., 2000; Sutton et al., 2009). The ratio of the number density of atomic oxygen to that of molecular nitrogen O/N_2 is a key parameter indicating the changes in thermospheric composition and essential for understanding ionospheric behavior in both quiet and disturbed conditions (Cai et al., 2021; Rishbeth, 1998). Several studies have reported a positive correlation between the O/N_2 ratio and electron density (Christensen, 2003; Fuller-Rowell et al., 1994).

The thermosphere-ionosphere system varies over different time scales, including a 27-day cycle linked to solar rotation. A delay from hours to a few days is observed in ionospheric parameters, such as total electron content (TEC), electron density and peak electron density (NmF2), in response to solar extreme ultraviolet (EUV) radiation (e.g., Jacobi et al., 2016; Ren et al., 2018; Schmölter et al., 2018, 2021) and modeling (e.g., Ren et al., 2018, 2019, 2020; Schmölter et al., 2020a, 2022; Vaishnav, Jacobi, et al., 2021; Vaishnav, Schmölter, et al., 2021; Vaishnav et al., 2018). This delay represents the time between peak solar radiation and the corresponding ionospheric response during the 27-day cycle. Previous investigations confirm that the ionospheric delay is due to increased atomic oxygen ion density in the F2 region (Jakowski et al., 1991; Schmölter & von Savigny, 2022), resulting from the ionization of atomic oxygen and photodissociation of molecular oxygen O_2 in the lower thermosphere. The delay arises due to an imbalance between ion production and loss processes (Ren et al., 2018). Transport processes and geomagnetic activity are key factors, with geomagnetic influence first suggested by Ren et al. (2018) and later confirmed by Schmölter et al. (2020b). Geomagnetic storms impact the structure of the upper atmosphere through processes such as Joule heating and the precipitation of auroral particles. This effects lead to variations in of TEC latitude and longitude, and change over time. With respect to the delayed ionospheric response, these interactions become particularly significant when geomagnetic activity-

driven TEC variations coincide with the peak of the solar EUV-driven 27-day rotation period. In such cases, the resulting TEC signature can be strongly affected, leading to greater variability in the observed delay.

Seasonal variations in ionospheric delay have been reported by Schmölter et al. (2020b). Vaishnav, Jacobi, Schmölter, and Dühnen (2024) explored the role of lower atmospheric forcing, suggesting its impact on ionospheric delay during low solar activity, especially in low and mid-latitudes. Schmölter et al. (2024) provided a comprehensive analysis, showing that ionospheric delay increases with solar activity. Additionally, Dühnen et al. (2024) found that long-term solar activity influences the accumulation of ionized species (O^+ and $O_2{}^+$) in the lower ionosphere at 230 km.

The delayed ionospheric response is influenced by multiple factors, including solar activity, lower atmospheric forcing, and geomagnetic activity. While previous studies have acknowledged the impact of geomagnetic activity on the ionospheric delay (Ren et al., 2018; Schmölter et al., 2020a, 2020b), significant gaps still exist in the understanding of its full spatiotemporal effects. For instance, Ren et al. (2018) analyzed electron density observations with Thermosphere-Ionosphere-Electrodynamics General Circulation Model (TIE-GCM: Richmond et al., 1992) simulations, demonstrated that geomagnetic activity reduces the ionospheric delay time. They found that the noontime NmF2 and TEC delays decreased from 0.8/0.7 days during quiet conditions to 0.6/0.5 days during geomagnetically active periods. Additionally, Schmölter et al. (2020b) identified seasonal and latitudinal variations in these delays and suggested a potential coupling with the 11-year solar cycle. Meanwhile, Schmölter et al. (2020a) quantified the dependency of the delay on geomagnetic activity intensity, noting increases from 15 to 17 hr as the Kp-index rose from 0.91 to 2.88 during December, highlighting the critical role of transport processes. Despite these, an exclusive model study investigating the impact of geomagnetic activity on ionospheric delay and its seasonal variations in ionospheric delay caused by geomagnetic activity is currently lacking. Therefore, in this work, we utilized TIE-GCM model simulations to further investigate how geomagnetic activity modifies the seasonal and spatial variability of ionospheric delays. We also explored the combined effects of geomagnetic storms occurring simultaneously with peak solar activity during solar rotation periods and aimed to distinguish geomagnetic effects from those driven by solar activity.

The model's capabilities in representing the thermosphere-ionosphere have been extensively studied for both quiet and disturbed conditions (Fernandez-Gomez et al., 2019; M. V. Codrescu et al., 2022; Shim et al., 2018), including studies on solar EUV-induced ionospheric delays (Schmölter et al., 2020a; Vaishnav, Schmölter, et al., 2021; Vaishnav et al., 2018) and diurnal tides (Fong et al., 2015). Shim et al. (2018) evaluated the performance of various ionospheric models, both empirical and physics-based, during the March 2013 storm, revealing location-dependent variations.

Using TIE-GCM simulations (2012–2013, 2015, 2023) and observational data, we analyze NmF2, TEC, O/N_2 ratios, F10.7, and geomagnetic indices to quantify the delayed ionospheric response under moderate geomagnetic disturbances. This work advances understanding of storm-time delay mechanisms and their dependence on seasonal and solar-geomagnetic coupling.

The manuscript is arranged as follows. Section 2 briefly introduces the data sources and the TIE-GCM. Section 3 describes the results, including observations and mechanistic model studies describing the influence of geomagnetic activity in the ionosphere and the effects of the ionospheric delay. Section 4 discusses our findings and concludes the paper.

2. Observations and Model

The ionospheric state as analyzed here is determined by measuring the TEC, continuously monitored by a global GNSS network and ionosondes (Hernández-Pajares et al., 2009). These measurements are available at a high temporal resolution (hourly) and a spatial resolution of 2.5° in latitude and 5° in longitude. We utilized NASA's 1-hourly global IGS TEC maps from the CDDIS data archive service (NASA, 2025a). The global mean TEC (GTEC) is calculated as an area-weighted average of vertical TEC values based on IGS TEC maps, using the cosine of the geographic latitude. The F10.7 index is often used as a proxy for solar activity, while the Kp index represents global geomagnetic activity, and we used daily values for both. The F10.7 index values can be accessed from the LISIRD database (LASP, 2025), while the Kp index values are obtained from the Omniweb database (NASA, 2025b).

In addition, we used GUVI O/N_2 observations from the TIMED satellite, which provides far ultraviolet spectra (115–181 nm) including the $Ly-\alpha$ line at 121.6 nm and N_2 LBH bands (Christensen, 2003). The O/N_2 ratio was derived using dayglow data at 135.6 nm, referencing a fixed N_2 column density of 1×10^{17} cm^{-2}. GUVI O/N_2 data sets are available at: http://guvitimed.jhuapl.edu/data/products (NASA, 2025c).

We conducted an analysis to investigate the impact of geomagnetic activity on the ionospheric delay mechanism using TIE-GCM version 2.0 simulations. This global, three-dimensional model of thermosphere-ionosphere electrodynamics effectively solves the continuity, momentum, and energy equations (Qian et al., 2014; Richmond & Maute, 2014). Our study utilized the model with a horizontal resolution of $5^\circ \times 5^\circ$ and a vertical resolution of 0.5 scale heights with an altitude range of 97–600 km. The lower boundary is set at a constant pressure level of about 97 km. For solar input, the model uses a reference solar spectrum from the EUVAC model (Richards et al., 1994).

In polar regions, TIE-GCM integrates high-latitude convection and auroral models, simulating magnetosphere-ionosphere coupling with ion convection patterns from Heelis et al. (1982) and auroral precipitation based on Roble and Ridley (1987). The aurora depends on the hemispheric power (hp), which the TIE-GCM estimates using a 3-hr Kp index. This study focuses on geomagnetic activity with Kp ≤ 7, using the model's calculated hp values by

$$hp = 16.82 \cdot e^{0.32 \cdot Kp} - 4.86. \quad (1)$$

Previous research has highlighted the significant impact of geomagnetic activity on the delayed ionospheric response (Ren et al., 2018; Schmölter et al., 2020b). Therefore, this study aims to reproduce these effects through model simulations and to examine the seasonal variations, along with the roles of solar and geomagnetic activity.

3. Results

3.1. Variations in Solar, Geomagnetic, and Thermosphere-Ionosphere Parameters

Figure 1a illustrates the variations of F10.7 and GTEC covering solar cycles 24 and 25. The GTEC changes with solar activity and also exhibits seasonal variations. We selected three 27-day time intervals for our investigation, each covering a clear solar irradiance cycle, which occurred in 2012–2013, 2023, and 2015, as shown in Figure 1a. These periods are as follows: Period 1 (28 December 2012–23 January 2013), Period 2 (2 January 2023–28 January 2023) and Period 3 (29 April 2015–25 May 2015). The purpose of using these periods is to understand the role of geomagnetic activity in the ionospheric delay.

The middle panels of Figure 1 illustrate the variations in solar and geomagnetic activity during selected periods. We specifically chose these periods based on the season and the levels of solar and geomagnetic activity observed at the peak of each solar rotation. To represent the solar activity, the F10.7 index is used while the Kp and Dst indices represent the geomagnetic activity. The considered time intervals, along with the central date characteristics of F10.7, Kp, the minimum Dst index and GTEC, are detailed for each cycle in Table 1.

During Period 1, moderate solar activity (F10.7 $\approx$168 sfu), and quiet geomagnetic activity were observed (Figure 1b). This period is considered as a reference because the geomagnetic activity is quiet (mean Kp $\approx$1 or Dst $\approx$1 nT) compared to the other two periods. In Period 2, solar activity was high and a few moderate storms were observed (Figure 1c). The minimum Dst during this period reached around -40 nT. The maximum F10.7 index was $\approx$227 sfu, while the minimum was $\approx$ 120 sfu. During Period 3, solar activity was similar to Period 1, with moderate geomagnetic activity indicated by a Dst index of about -33 nT, and the minimum Dst during this period reached around -60 nT (Figure 1d). The observed GTEC values during peak solar activity days for periods 1, 2, and 3 are approximately 24.52, 33, and 30 TECU, respectively (see Table 1).

TEC or NmF2 are typical parameters used to describe the ionospheric conditions. The observed zonal mean TEC variations for the selected study periods are shown in the corresponding lower panels of Figure 1. The ionospheric TEC varies both spatially and temporally depending on solar and geomagnetic activity conditions. During Period 1, the TEC values show less fluctuation and reach a maximum of about 30 TECU in the low-latitude region.

In contrast to Period 1, Period 2 exhibits strong TEC fluctuations and a generally higher TEC level, reaching a maximum of 45 TEC. Seasonal variations are also evident during these periods, with Periods 1 and 2 representing

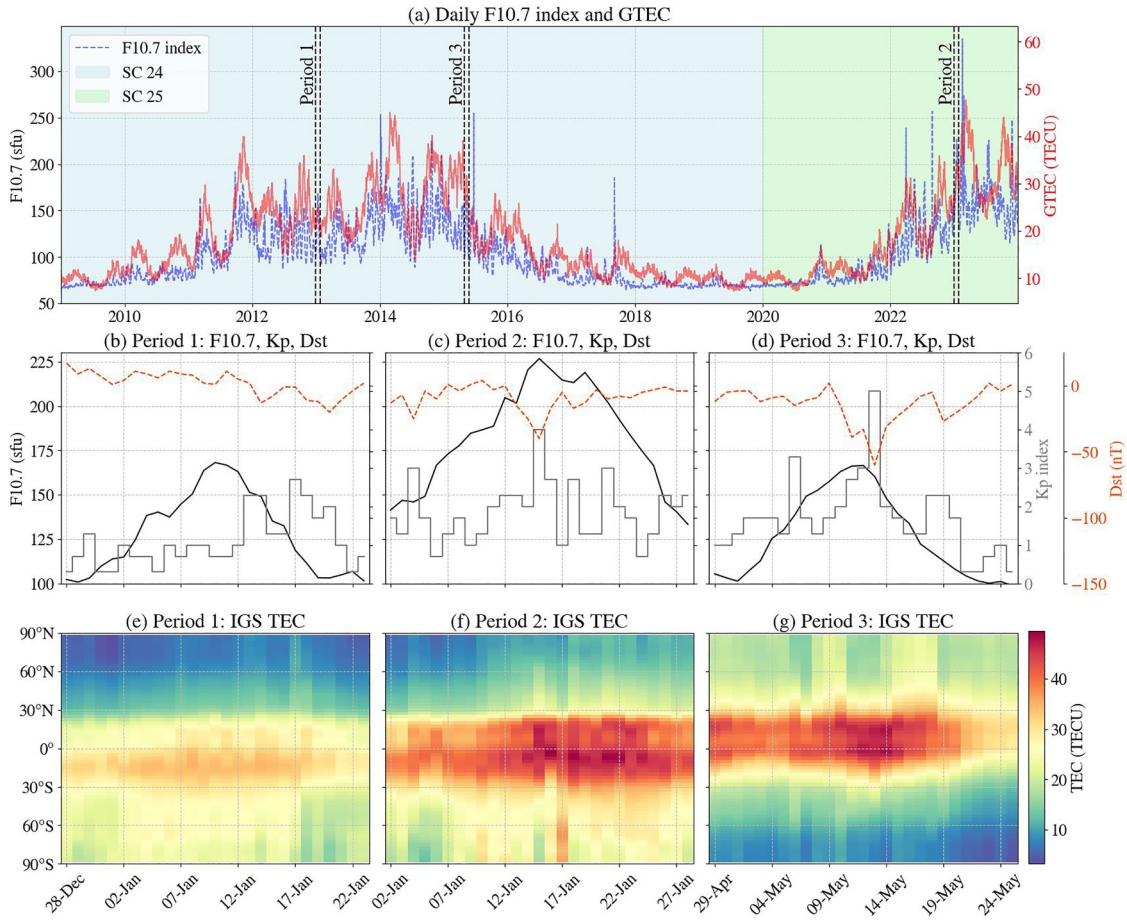

Figure 1. The time series of F10.7 and GTEC is presented from 2009 to 2023, with vertical dashed black lines indicating the study periods The time series of the F10.7, Kp and Dst indices are presented for (b) Period 1 (28 December 2012–23 January 2013), (c) Period 2 (2 January 2023–28 January 2023), and (d) Period 3 (29 April 2015–25 May 2015) are shown in middle panel. The lower panels (e, f, g) display the corresponding zonal and daily mean observed IGS TEC variations, organized by day and latitude.

the Northern Hemisphere (NH) winter, and Period 3 representing the Southern Hemisphere (SH) winter. This will help to investigate the hemispheric differences during the study periods.

We also examined the relationship between TEC and solar and geomagnetic activity using conditional correlation analysis, which eliminates the influence of respective factors. The left column of Figure 2 shows the correlation between observed TEC and the F10.7 index during Periods 1, 2, and 3, respectively. During Period 1, geomagnetic activity was quite low, resulting in a relatively stronger influence of solar variations and consequently a generally higher correlation observed in the low and mid-latitude regions and at the geomagnetic equator, with coefficients around 0.9. However, there was a lower correlation, about 0.5, observed around the equator in the Pacific region and in the NH. The maximum correlation was seen in the SH compared to the NH. In Period 2, the overall correlation coefficients are slightly decreased compared to Period 1. The maximum

Table 1
The F10.7 Index, Geomagnetic Activity Indices, and GTEC for Central Dates During Selected Time Intervals in 2012–2013, 2015, and 2023

No.	Time interval	Central date	Central date characteristics			
			F10.7 (sfu)	Mean Kp index	Minimum Dst (nT)	GTEC (TECU)
1	28 December 2012–23 January 2013	11 January 2013	168	1	1	24.52
2	02 January 2023–28 January 2023	15 January 2023	227	4	−40	33.02
3	29 April 2015–25 May 2015	10 May 2015	167	3	−33	30.30

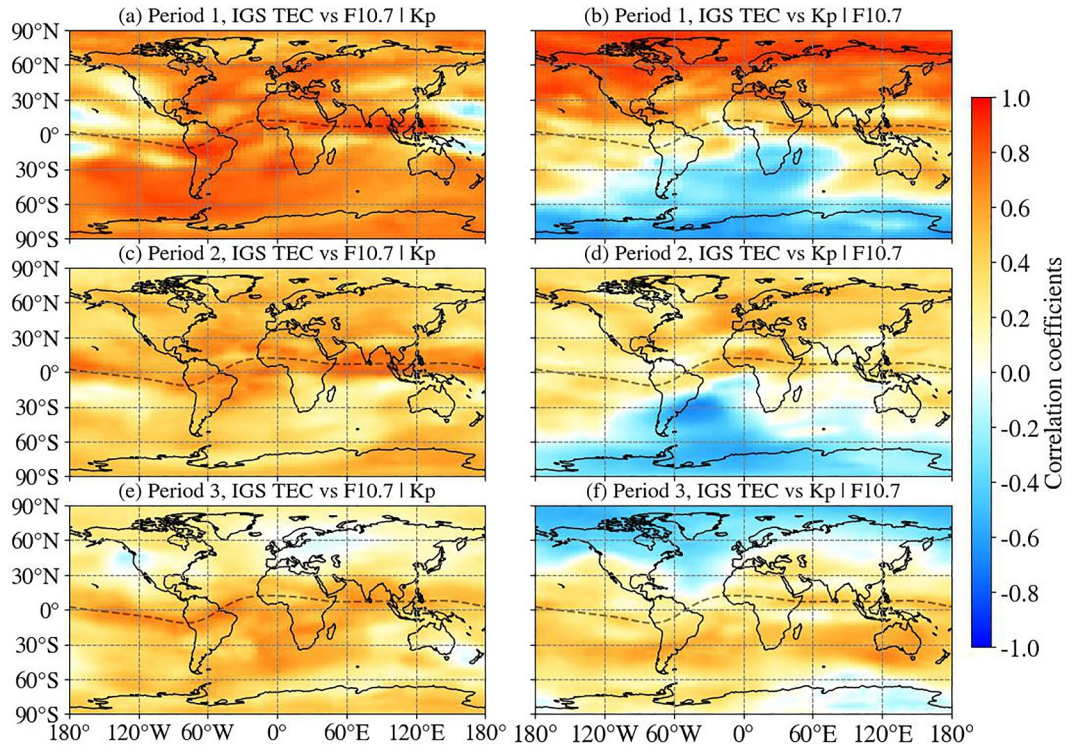

Figure 2. The spatial distribution of conditional cross-correlation coefficients between IGS TEC and F10.7/Kp indices is presented for (a, b) Period 1 (28 December 2012–23 January 2013), (c, d) Period 2 (2 January 2023–28 January 2023), and (e, f) Period 3 (29 April 2015–25 May 2015). The left panels show the conditional correlation between IGS TEC and the F10.7 index, while the right panels show the correlation with the Kp index.

correlation coefficient is approximately 0.7 at the equator, while the correlation slightly decreased in the SH. As in Period 1, the correlation coefficients over the NH continents and Atlantic sector are higher than over the Pacific. This may be due to the less dense IGS receiver network across the Pacific compared to the Atlantic sector, resulting in fewer TEC measurements. Additionally, there may be some unusual effects from satellite measurements interacting with the background model (e.g., Hernández-Pajares et al., 2009).

Overall positive correlation observed as this period is highly dominated by the solar activity. During Period 3, a positive correlation of about 0.5 was observed in the SH, at low latitudes and at lower mid-latitude regions of both hemispheres, while a negative correlation appeared in the NH at mid-latitudes.

The right column of Figure 2 shows the spatial distribution of correlation coefficients between the Kp index and observed TEC, thus investigating the geomagnetic activity response during the respective periods. Figure 2a indicates strong correlation in the NH and negative correlation in the SH during Period 1, showing asymmetry between summer and winter hemispheres. During this period, geomagnetic activity was low and primarily influenced by solar activity. However, the maximum correlation coefficients between Kp and TEC were still observed at NH high latitudes (Figure 2b). Similarly, during Period 2, we noted a qualitatively almost identical TEC response to Kp compared to Period 1, although especially the NH with slightly lower correlation (Figure 2d). This suggest that the correlation between Kp and TEC becomes essentially stronger at lower solar flux (see Figure 2b). In Period 3 (Figure 2f), the maximum correlation was observed in the SH, in contrast to the high latitudes of the NH. A negative correlation ranging from 0.2 to 0.6 is noted in the high latitudes and partially in the mid-latitudes of the NH.

Overall, the conditional correlation analysis between solar activity and IGS TEC across all periods shows a similar spatial distribution, although the magnitudes differ. Additionally, differences in correlation have been noted between the IGS TEC and the Kp index in different hemispheres. This analysis suggests the varying contributions of solar and geomagnetic activity under different solar and geomagnetic conditions.

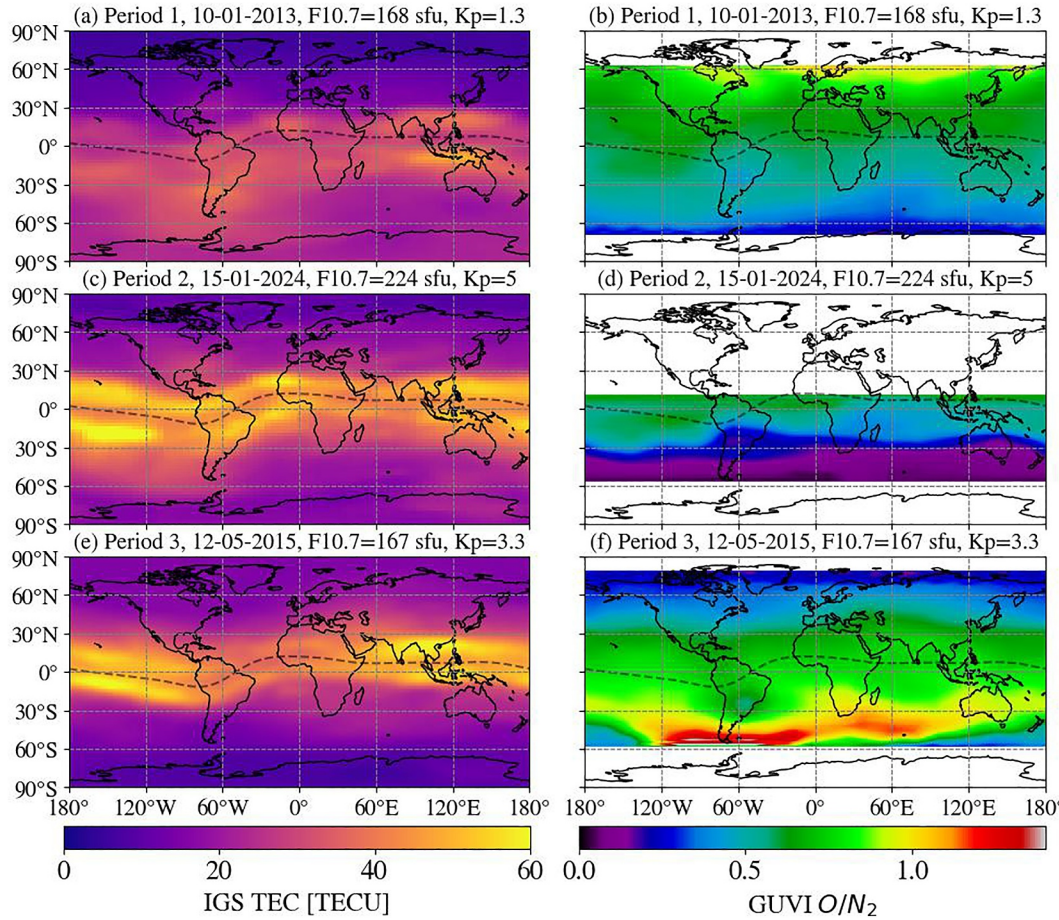

Figure 3. The left panels show the spatial distribution of the IGS TEC, while the right panels display the spatial distribution of the TIMED GUVI O/N_2 ratio. These distributions are presented for the central date of (a, b) Period 1 (10 January 2013), (c, d) Period 2 (15 January 2023), and (e, f) Period 3 (12 May 2015).

To investigate the role of solar and geomagnetic activity on ionospheric variability, we discuss the evolution of observed TEC and O/N_2 ratio. Figure 3 illustrates the spatial distribution of observed daily TEC and the GUVI observed O/N_2 ratio during the peak solar activity day (day 14 of the respective solar rotation period). Figures 3a, 3c, and 3e display the observed TEC.

Among the three periods analyzed, solar activity during Period 2 was notably high, with TEC peaking at approximately 55 TECU during this peak solar activity. In Period 3, the solar activity was about 167 sfu, comparable top Period 1 and lower than during Period 2. The TEC in Period 2 was somewhat reduced compared to Period 2's peak, but remained at the same order of magnitude. When compared to Period 1, the TEC values are significantly higher; however, this difference could be attributed to seasonal variations and moderate geomagnetic activity. Reflecting the seasonal variation, during Period 3 the high latitude SH/NH TEC values are lower/larger than during Periods 1 and 2. Overall, the distribution remains consistent, with magnitude differences influenced by solar and geomagnetic activity, as well as seasonal anomalies.

The right panel of Figure 3 displays the GUVI O/N_2 ratio during the peak solar activity day of the respective periods. The evolution of O/N_2 indicates that during Period 1, the maximum O/N_2 was observed in the NH, with lower values in the SH. This trend continued during Period 2; however, due to moderate geomagnetic activity, the O/N_2 ratio decreased in the high-latitudes of the SH. In contrast to Periods 1 and 2, the maximum O/N_2 ratio during Period 3 was observed in the SH. The increase in the O/N_2 ratio may also be a result of moderate geomagnetic activity.

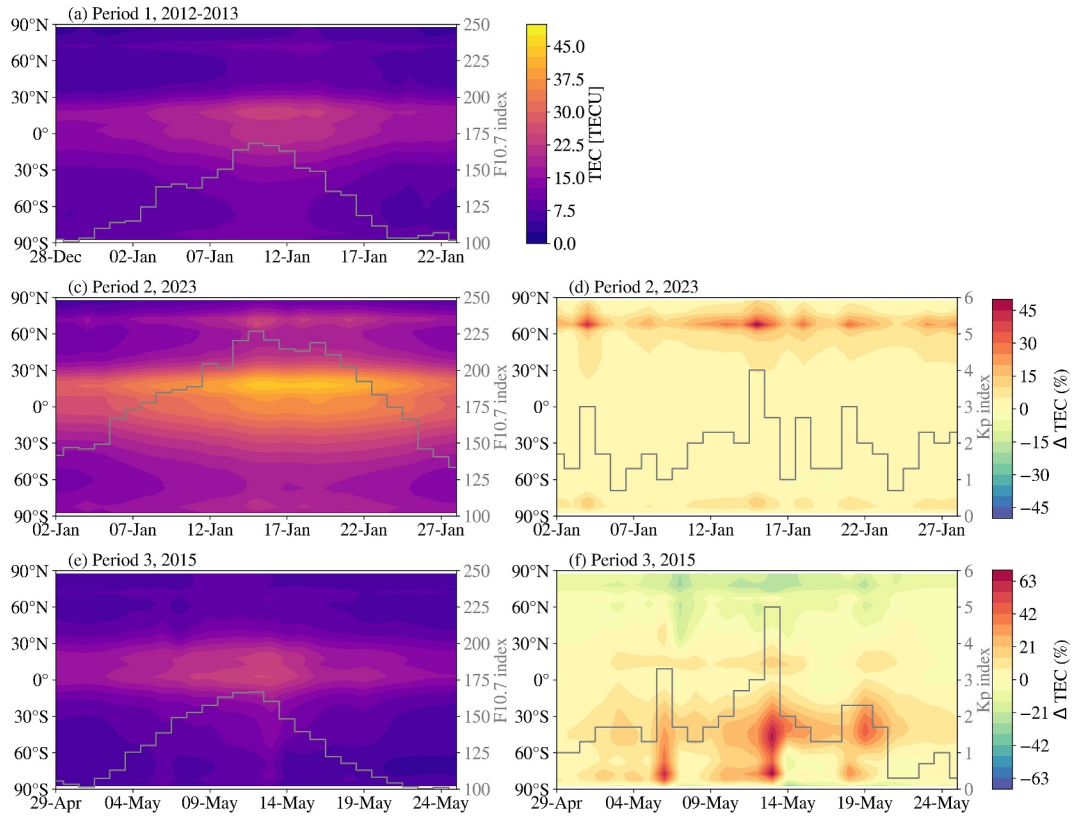

Figure 4. Modeled TEC variations, as a function of day and latitude simulated for (a, c, e) Solar Variability Run, and (d, f) percentage difference ((All Variability − Solar Variability)/Solar Variability) between Solar and All Variability Run at 0° longitude. The right y-axis in each panel represents the F10.7 (Kp) index in left and right panels. Geomagnetic activity during Period 1 was quiet, resulting in minimal differences between the Solar Variability Run and the All Variability Run. Thus, we did not show a difference plot for this period.

The O/N_2 ratio reflects changes in composition during geomagnetic activity and is crucial for understanding variations in ionospheric plasma density. Therefore, we will further examine the model-simulated TEC and O/N_2 response to explore the influence of geomagnetic activity on the delayed response of the ionosphere.

3.2. Mechanistic Model Studies

In this study, we conducted several experiments using the TIE-GCM model to examine the impact of geomagnetic activity in conjunction with solar activity, without modifying the lower boundary. Below are the runs we executed to showcase this effect.

1. All Variability Run: The model was run with the default setting (mentioned in the data section), observed F10.7, and observed Kp index.
2. Solar Variability Run: The model was run with the default setting, observed F10.7, and for Kp = 0.

Figure 4 shows the impact of geomagnetic activity over the three selected study periods. The left panel displays the All Variability Run, while the right panel shows the difference between the All Variability Run and the Solar Variability Run. Additionally, the F10.7 (Kp) index is included on the second y-axis in the left (right) panel. Figure 4a illustrates the evolution of TEC during Period 1 for All Variability Run. The TEC values correlate with solar activity, peaking in the low-latitude region. Since geomagnetic activity during this period has been very quiet, differences between the Solar Variability Run and the All Variability Run are minimal, and we refrained from showing them in the figure.

Figure 4c shows TEC variations during Period 2, characterized by high solar activity, resulting in a TEC enhancement. The maximum TEC in the low-latitude region reaches about 50 TECU during peak solar activity.

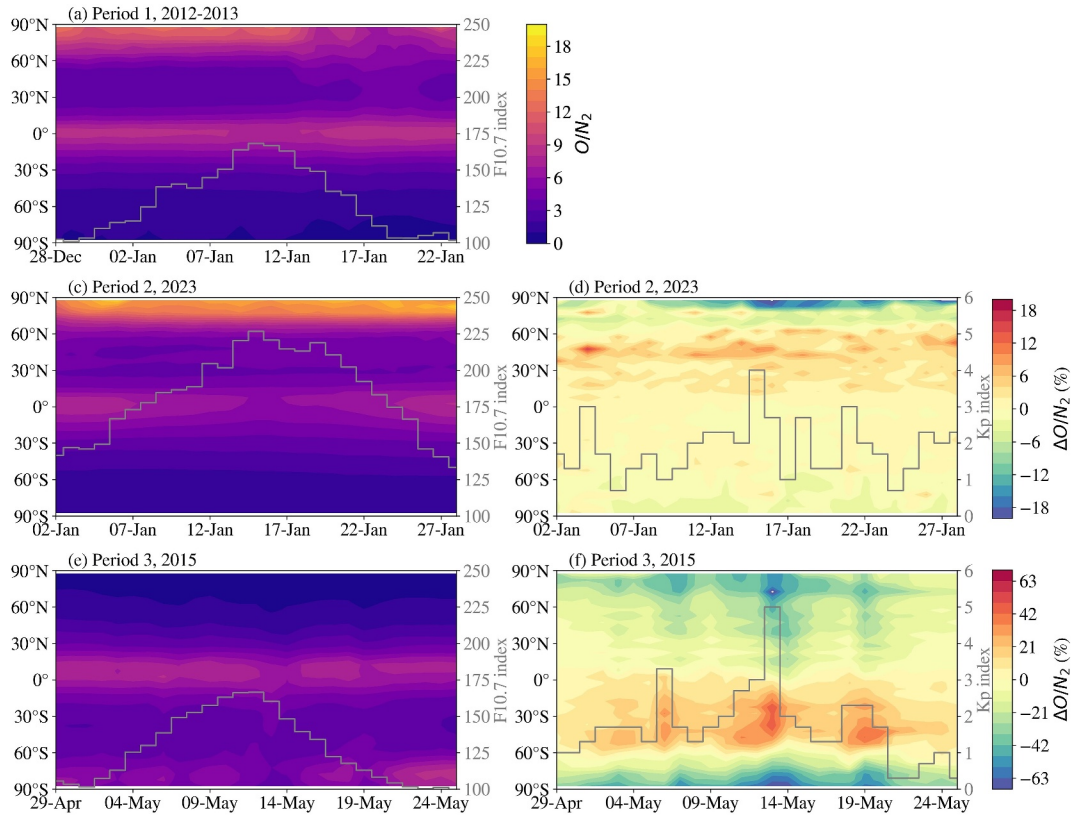

Figure 5. Modeled O/N_2 variations, as a function of day and latitude simulated for (a, c, e) Solar Variability Run, and (d, f) relative difference between All Variability and Solar Run at 0° longitude. The right y-axis in each panel represents the F10.7 (Kp) index in left and right panels.

With moderate geomagnetic activity in Period 2, we also performed simulations for the Solar Variability Run. The percentage difference plot, ((All Variability − Solar Variability)/Solar Variability) (Figure 4d), shows a moderate TEC enhancement of approximately 20% in the NH between 60°N and 80°N. During this period, solar activity predominates, with relatively small impact from geomagnetic activity.

Figure 4e shows the TEC variations during Period 3. The TEC variations are similar to those of Period 1, with maximum values of about 25 TECU observed in the low-latitude region during peak solar activity. Figure 4f illustrates the difference plots indicating a 20%–50% increase in the SH, particularly during intervals of moderate geomagnetic activity (gray curve). With moderate solar and geomagnetic activity, the influence of geomagnetic activity is clearly evident in the difference plot. Similar differences has been seen in when investigating NmF2 instead of TEC (Figure not shown).

The daytime electron density depends on the neutral species (O, N_2, and O_2), and the electron density N can be expressed as follows (Rishbeth, 1998):

$$N \sim \frac{q}{\beta} \sim \frac{I[O]}{\gamma_1[N_2] + \gamma_2[O_2]}\,. \tag{2}$$

In Equation 2, q represents the production term, β is the loss term, I denotes the solar ionizing flux, and γ_1 and γ_2 are the reaction rates, respectively. Equation 2 indicates that the electron density primarily depends on the O/N_2 ratio. Therefore, we calculate the modeled O/N_2 ratio.

Figure 5 shows the variations in the modeled O/N_2 ratio, which, for low- and midlatitudes, resemble the TEC during the selected periods. The maximum O/N_2 ratios during Periods 1 and 2 are observed in the high-latitude

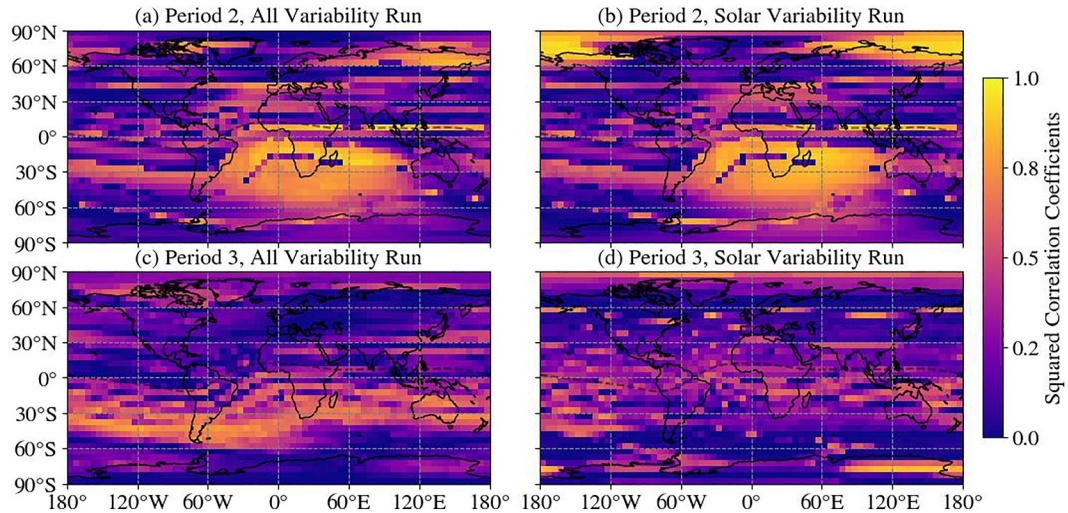

Figure 6. Squared correlation coefficients between modeled NmF2 and the corresponding O/N_2 ratio for (a, c) All Variability Run and (b, d) Solar Variability Run during Period 2 (a, b) and Period 3 (c, d).

NH, unlike the SH (see Figures 5a and 5c). However, during Period 3, a high O/N_2 ratio is noted in the SH (Figure 5e). This variation is attributed to seasonal changes in the O/N_2 ratio.

The difference plot for Period 2 indicates minimal O/N_2 changes in the NH due to the dominant solar activity. In contrast, Period 3 shows significant differences, positive in the SH and negative in the NH. At high latitudes, negative relative differences are seen in both hemispheres. The differences observed in both the TEC and O/N_2 ratio can be attributed to geomagnetic activity.

This study demonstrates the model's reproduction of TEC and the O/N_2 ratio during geomagnetic activity changes, highlighting the role of geomagnetic activity in ionospheric variability. Fang et al. (2018) previously examined diurnal variability in June–July 2012 using WAM-GIP model simulations, finding that relative TEC variability is mainly influenced by geomagnetic activity, followed by solar activity and lower atmospheric perturbations. These findings also suggest that geomagnetic activity plays a significant role in ionospheric behavior, although further investigation, accounting for other factors, is needed.

Given the significant dependence of electron density variations on neutral composition, we investigate the combined effects of solar and geomagnetic activity by analyzing NmF2 and the O/N_2 ratio at hmF2 (the peak height of the F2 region). We use NmF2 rather than TEC because as it better isolates F2-layer processes affected by composition changes, and maintains a strong linear relationship with TEC ($r \geq 0.85$), as demonstrated in prior studies (Houminer & Soicher, 1994; Kouris et al., 2004; Krankowski et al., 2007; Y. Yu et al., 2013).

By comparing NmF2–O/N_2 correlations between the All Variability and Solar Variability runs, we quantify how geomagnetic forcing modifies plasma-neutral coupling. This approach reveals the dominant role of storm-induced O/N_2 changes in altering electron density under both moderate and strong solar activity conditions.

Figure 6 illustrates the squared correlation coefficients between the modeled NmF2 and the corresponding O/N_2 ratio during Periods 2 and 3 for both the All Variability Run and the Solar Variability Run. During Period 2, the squared correlation shows little difference between the two runs, except for increases in correlation observed in NH high-latitudes in the Solar Variability Run compared to the All Variability Run (Figures 6a and 6b). This is NH winter, so the higher correlation is probably due to indirect solar effects or transport processes.

In contrast, during Period 3, geomagnetic activity plays a significant role and its influence cannot be ignored. Figures 6c and 6d shows the squared correlation coefficients for both the All Variability Run and the Solar Variability Run during Period 3. The comparison reveals changes in correlation coefficients in the SH, with a decrease in the Solar Variability Run relative to the All Variability Run. This indicates the dominant effects of geomagnetic activity over solar activity during Period 3.

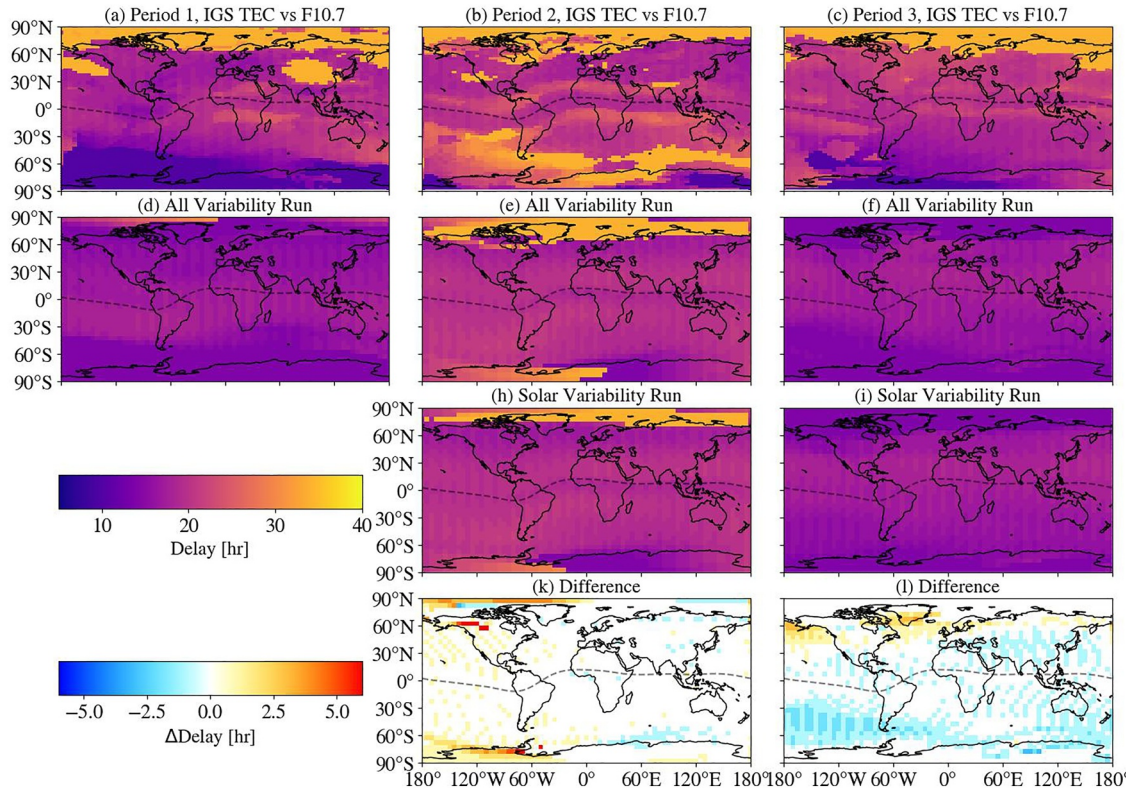

Figure 7. The spatial distribution of ionospheric delay is estimated between the F10.7 index and the observed or modeled TEC. The upper panels illustrate the delay between the observed TEC and the F10.7 index over three selected periods: (a) Period 1, (b) Period 2, and (c) Period 3. The second row features the modeled delay for the All Variability Run, shown in panels (d)–(f). Additionally, the third row presents the Solar Variability Run for Periods 2 and 3, as depicted in panels (h) and (i), respectively. Finally, the lower panels (j) and (k) show the differences (All-Solar Variability Run) between the All Variability Run and the Solar Variability Run for Periods 2 and 3.

3.3. Delayed Ionospheric Response

To assess the impact of geomagnetic activity on the delayed response of the ionosphere, this study will utilize TIE-GCM simulations, as described in Section 3.2. We calculated the ionospheric delays in TEC for the three periods mentioned earlier by using cross-correlation analysis between hourly TEC data and the F10.7 index, which serves as a standard proxy for solar activity. As noted in Vaishnav, Jacobi, Schmölter, and Dühnen (2024), a comparison of ionospheric delay calculated between TEC with both EUV and the F10.7 index revealed similar results. Therefore, in this study, we opted to use the F10.7 index to calculate the ionospheric delay with observed and modeled TEC. To align the TEC time series with the F10.7 index, we linearly interpolated the F10.7 index to a 1 hr resolution. Although this interpolation may introduce minor artifacts in the absolute values of cross-correlation, it maintains the accuracy of relative lag timing. This method has been validated in prior studies (Schmölter et al., 2024; Vaishnav, Jacobi, Schmölter, & Dühnen, 2024; Vaishnav, Jacobi, et al., 2021).

The spatial distribution of the delay is shown in Figure 7. The upper row illustrates the ionospheric delay between observed TEC and the F10.7 index for all three periods. During the first period, the ionospheric delay was approximately 17 hr, with a longer delay observed in the NH's high-latitude region, ranging from 30 to 40 hr. In contrast, the SH's high-latitude region exhibited a shorter delay of about 1–5 hr. In the mid-latitude regions, the average delay was around 12–20 hr. A similar characteristic can be seen in the model-simulated latitudinal distribution of TEC delay for the All Variability Run, though with differences in magnitude. The average delay in the model-simulated data is approximately 18 hr. We did not calculate the delay for the Solar Variability Run, as geomagnetic activity was relatively low during this period.

In comparison to Period 1, there is an observed delay of approximately 24 hr during Period 2. This increase in delay is expected due to higher solar activity during this period (see Figure 7b). Additionally, hemispheric differences are evident in the high-latitude regions, with a greater delay observed in the SH compared to the NH.

When examining the delay in TEC, the modeled TEC from the All Variability Run shows similar trends, although with slight differences in magnitude (Figure 7e). Recently, Schmölter et al. (2024) investigated the ionospheric delay under different solar activity conditions. They found that the ionospheric delay increases with higher solar activity.

Given the active geomagnetic conditions during Period 2, we also calculated the delay for the Solar Variability Run (illustrated in Figure 7h). The lower panel depicts the difference between the modeled delays for the All Variability Run and the Solar Variability Run. This difference plot highlights the contribution of geomagnetic activity to the ionospheric delay. The results indicate an overall small increase in the ionospheric delay of about 1–3 hr in the Western Hemisphere midlatitudes, while the Eastern Hemisphere experiences a slight decrease. At polar latitudes the changes are larger.

The third column of Figure 7 shows the ionospheric delay for Period 3. The solar activity during this period is quite similar to that of Period 1. Consequently, the spatial distribution of the ionospheric delay also resembles that of Period 1. However, there are some differences in the high-latitude regions (see Figure 7c). Figures 7f and 7i display the delay for the All Variability and Solar Variability Runs, respectively. The difference between these two runs is illustrated in Figure 7l. The results suggest that due to geomagnetic activity, there is a decrease in delay of about 1–3 hr, except in the NH high-latitude region, where the delay increases by about 1–4 hr.

The difference plot for Periods 2 and 3 illustrates the varying characteristics of ionospheric delay influenced by geomagnetic activity and solar activity. During Period 2, there is high solar activity and moderate geomagnetic activity, which results in differences between the Eastern and Western Hemispheres. In contrast, during Period 3, with moderate solar and moderate geomagnetic activity, there is a slight increase in ionospheric delay in the NH's high-latitude region, while delays decrease in other latitudes.

This study demonstrates that the ionospheric delay varies with moderate geomagnetic activity. The findings align with prior research by Vaishnav, Schmölter, et al. (2021).

To effectively evaluate the performance of the TIE-GCM simulations in both the All Variability Run and the Solar Variability Run, we calculated the mean absolute error (MAE) of modeled against IGS TEC delay, which have been illustrated in Figure 7.

The ionospheric delay presents variability across different regions, which is an important consideration in our analysis. As a result, we have computed the MAE values for a grid resolution of 2.5°/5° in latitude and longitude, and the modeled delay is interpolated to this grid for comparison with the observations. Figure 8 offers a comparison of these MAE values, showcasing the differences between the observed and modeled delays. The upper panels of Figure 8 illustrate the MAE between both the observed and modeled delays, calculated using the F10.7 index during Period 1, as referenced in Figures 7a and 7d. During Period 1, the MAE between the IGS and the All Variability Run is approximately 5 hr. For low- and mid-latitude regions, the MAE value is around 3.3 and 3 hr, while for high-latitude region, it increases to about 7 hr (Figure 8a). Since geomagnetic activity was quiet during this period, the Solar Variability Run is not shown here.

Figures 8c and 8d display the MAE for the All Variability Run and the Solar Variability Run during Period 2, respectively. The MAE between the IGS observed global delay and the estimated global delay from the All Variability Run is approximately 4.4 hr (Figure 8c). In comparison, the MAE for the Solar Variability Run is about 6.6 hr (Figure 8d). When examining low- and mid-latitude regions, we find that the MAE for the All Variability Run is around 2.8 and 3.7 hr, while the Solar Variability Run shows an MAE of approximately 5.3 and 5.9 hr. In high-latitude regions, the MAE increases to about 7 hr for the All Variability Run and 9 hr for the Solar Variability Run.

The lower panels of Figure 8 display the MAE values during Period 3. The MAE for the All Variability Run at a global level is about 3 hr (Figure 8e), while the Solar Variability Run, it is about 3.5 hr (Figure 8f). For the low- and mid-latitude regions, the MAE values of approximately 1 and 2 hr, respectively for All variability Run while 2 and 3 hr for Solar Variability Run. Similar to Period 2, high-latitude region show an increase in MAE, reaching about 5.8 hr for the All Variability Run and 6.4 hr for the Solar Variability Run.

During Period 3, the All Variability Run showed a MAE of about 5–10 hr larger in the mid- and high-latitude regions of the NH, highlighting a hemispheric asymmetry. In contrast, the MAE in the SH remains below 5 hr.

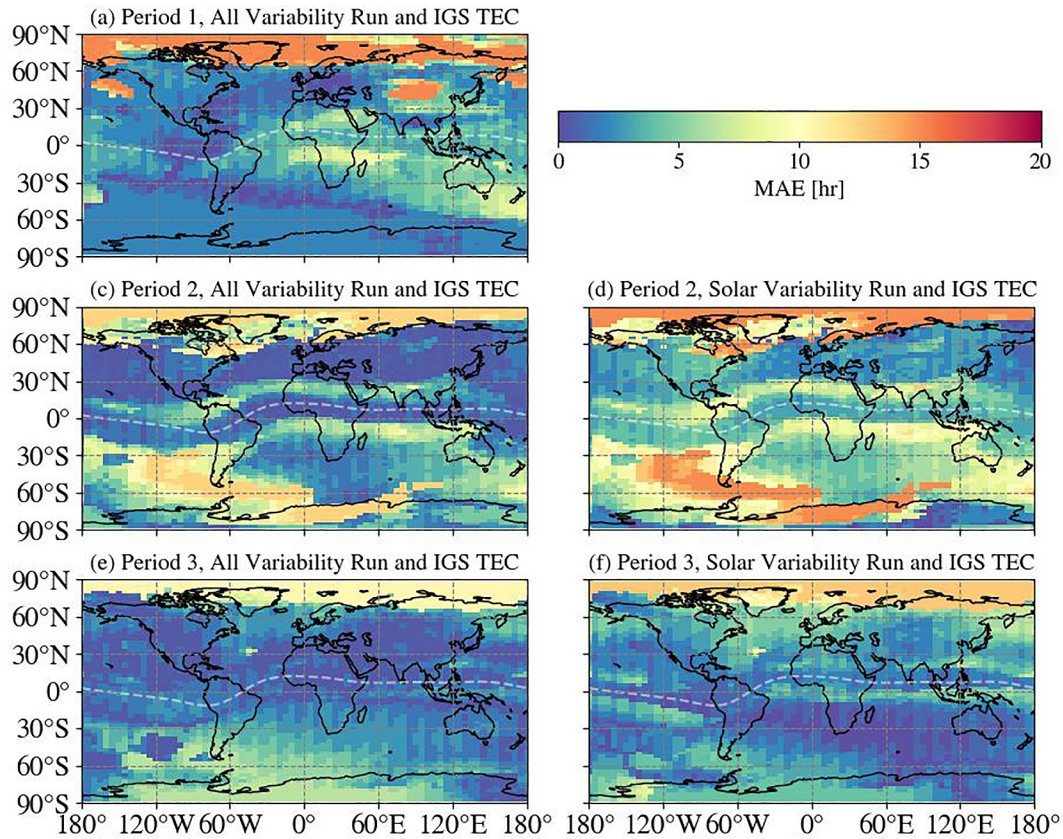

Figure 8. The MAE maps are presented as follows: Panels (a, c, f): IGS and TIE-GCM modeled delays for the All Variability Run using F10.7 for Periods 1, 2, and 3, respectively. Panels (d, f): IGS and TIE-GCM modeled delays for the Solar Variability Run using F10.7 for Periods 2 and 3, respectively. The MAE values are calculated at a grid resolution of 2.5° in latitude and 5° in longitude.

The MAE analysis for Periods 2 and 3 allows us to compare the impact of geomagnetic activity across two different seasons. During Period 2, solar activity is dominant compared to Period 3, which is reflected in the MAE analysis. In Period 2, the MAE in the low- and mid-latitude regions is approximately 6 hr for the Solar Variability Run and 4 hr for the All Variability Run. This indicates that including geomagnetic activity reduces the delay in the low- and mid-latitude regions by about 2 hr. Conversely, during Period 3, when solar activity is weaker than in Period 2, the MAE values decreases. In the All Variability Run, the MAE is about 2 hr, compared to about 3 hr in the Solar Variability Run.

Overall, for all three selected periods, the MAE values are larger in the high-latitude region compared to the low- and mid-latitude regions. This reflects the difficulty of TIE-GCM in reproducing the highly variable ionospheric conditions in these regions, which are strongly influenced by particle precipitation, auroral electrodynamics, and geomagnetic variations. Furthermore, the model's spatial resolution and reliance on the empirical Heelis convection model (driven by 3-hr Kp) limit its ability to capture small-scale or rapidly varying processes, leading to larger discrepancies with observations (M. Codrescu et al., 2000; Günzkofer et al., 2024, 2025).

Schmölter et al. (2020b) focused on the seasonal variations of ionospheric delay and suggested that geomagnetic activity plays a significant role in explaining these variations. To investigate the influence of geomagnetic activity on seasonal variations, we performed additional model simulations for Period 1 and Period 3, and varied the levels of geomagnetic activity (Kp = 3, 5, and 7) with lags of 0, 1, −1, and −2 days, as sketched in Figure 9. We introduced these lags, as it may take up to 2 days for the ionosphere to return to the previous state after a geomagnetic disturbance (Yao et al., 2016). A lag 0 indicates increased geomagnetic activity on the day of maximum solar activity during the solar rotation period. Lag 1 refers to one day after the maximum solar activity, while lags −1 or −2 indicates one or 2 days, respectively, before the day of maximum solar activity. The analysis

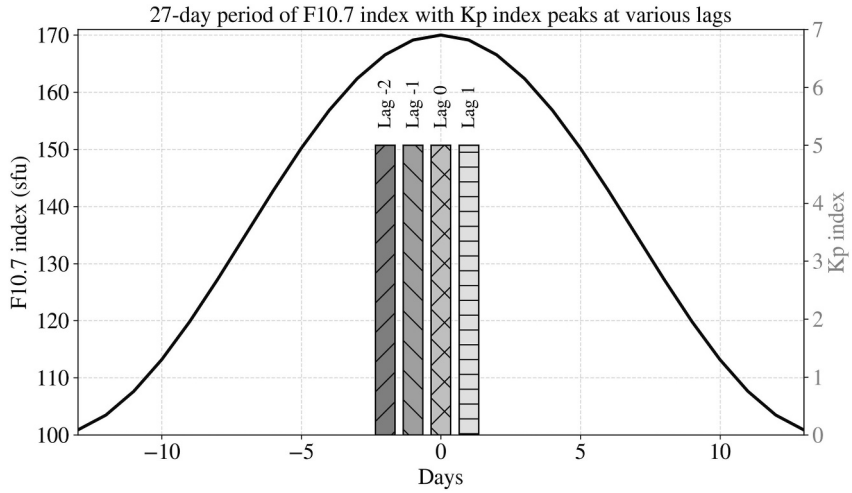

Figure 9. An illustration of variations in solar F10.7 over 27 days, along with the Kp index (e.g., Kp = 5), at different lag times of 0, 1, −1, and −2 days.

of Kp lags (0, 1, −1, −2 days) reveals distinct phases of ionospheric response to geomagnetic forcing: (a) preconditioning (−2/−1 day lags), where storm-induced O/N_2 depletion (Fuller-Rowell et al., 1994; Strickland et al., 2004) and disturbance dynamo winds (Blanc & Richmond, 1980) preconfigure the thermosphere to amplify or suppress subsequent solar flux effects; (b) direct coupling (lag 0), dominated by prompt penetration electric fields and Joule heating (Rishbeth et al., 2000); and (c) recovery (+1 day), governed by neutral wind circulation (T. Yu et al., 2022). As mentioned above, recovery (+1 day) usually describe the ionospheric recovery following the F10.7 maximum. However, if a geomagnetic storm begins on day +1, this interval instead reflects the storm's main phase or onset, rather than a recovery from solar EUV forcing.

Notably, the improved TEC-F10.7 correlation at −1 day lag may arise when storm-driven plasma transport preenhances electron density, creating optimal conditions for later solar ionization, which probably results in negative delays. This reflects the storm-driven ionospheric response rather than the intrinsic Sun–ionosphere relationship. While lags generally capture the delayed ionospheric response to solar activity, extreme geomagnetic events can modulate the apparent lag. Recent studies (Schmölter et al., 2024) also found negative delay in the high latitude region that was possibly caused by the geomagnetic activity and other high latitude processes. Therefore, the current analysis would be helpful to investigate the contribution of geomagnetic activity in the ionospheric delay.

Figure 10 shows the effects of geomagnetic activity on the ionospheric delay. The upper panels display the spatial distribution of ionospheric delay between the modeled TEC and the F10.7 index during Period 1 for Kp values of 3, 5, and 7 at lag 0. The distribution of ionospheric delay is quite similar across these Kp values. However, an increase in geomagnetic activity results in slight decreases in the ionospheric delay at higher latitudes. The average delay is approximately 17, 18, and 19 hr, with maximum delays observed in the mid-latitude and low-latitude regions.

The second row (Figures 10d–10f) shows the differences between the lag 0 and lag 1 cases for the respective geomagnetic activity. The results indicate that under lag 1 conditions, differences between the eastern and western Hemispheres are observed in the SH. The ionospheric delay decreases in the NH as well as in the western hemisphere of the SH, with a reduction of about 1–3 hr. In contrast, the delay in the eastern Hemisphere of the SH increases by approximately 1–3 hr. Additionally, the delay difference increases with geomagnetic activity, with the exception of the western SH high latitudes, where the delay difference increases in magnitude for Kp = 5, but decreases again for Kp = 7.

The third row (Figures 10g–10i) shows the differences between the lag 0 and lag −1 cases for the respective geomagnetic activity. The results show exactly the opposite distribution of the one for lag 1, with an almost similar magnitude. The results for lag −2 (lower row of Figure 10) shows the same spatial distribution of differences than lag −1, but with increasing magnitude.

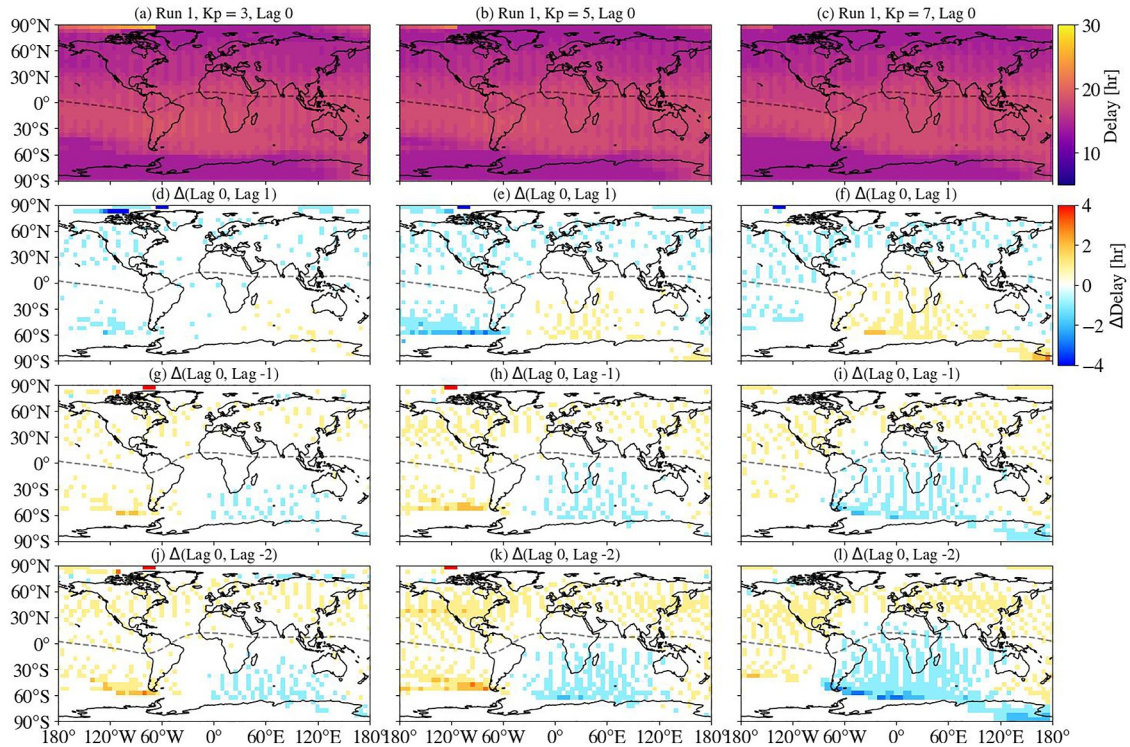

Figure 10. Upper Panels: The spatial distribution of ionospheric delay is estimated using the F10.7 index and modeled TEC for (a) Kp = 3, (b) Kp = 5, and (c) Kp = 7, at lag 0 for Period 1. Second Row: The corresponding delay differences between lags 0 and 1. Third Row: Delay differences between lags 0 and −1. The lower Panels (j, k, l) indicate the delay differences between lags 0 and −2. Positive values indicate increase of the delay with respect to the case with lag 0.

Figure 11 illustrates the effects of geomagnetic activity on ionospheric delay during Period 3 under different geomagnetic activity conditions. Compared to Period 1, we anticipate a hemispheric difference due to seasonal variations between the study periods. Figures 11a–11c displays the variations in geomagnetic activity for Kp values of 3, 5, and 7 under lag 0 conditions. The second row presents the difference between the lag 0 and lag 1 conditions. The difference plots clearly indicate an increase in delay in the NH, while a decrease is observed in the SH, amounting to approximately 1–2 hr. These differences increase with higher geomagnetic activity (Figures 11d–11f). In contrast to lag 1, lag −1 exhibits opposite hemispheric behavior, which is expected. Lag −2 (lower row of Figure 11) again shows the same spatial distribution of differences than lag −1, with increasing magnitude.

4. Discussion and Conclusions

To understand the impact of geomagnetic activity on ionospheric delay, we conducted a comprehensive investigation of the Total Electron Content (TEC) predictions during several specific 27-day time intervals. These are: Period 1 (28 December 2012–23 January 2013), Period 2 (2 January 2023–28 January 2023), and Period 3 (29 April 2015–25 May 2015). To achieve this, we utilized the Thermosphere-Ionosphere-Electrodynamics General Circulation Model (TIE-GCM) to simulate various ionospheric and thermospheric parameters, alongside the observed O/N_2 ratio and the International GNSS Service (IGS) TEC data. To investigate the effects of geomagnetic activity, we ran the model using two different conditions: one run included all sources of variability (both solar and geomagnetic activity; "All Variability Run") and another one without geomagnetic activity, which therefore considered only solar variability ("Solar Variability Run").

The ionospheric delay calculated using the observed TEC and F10.7 values aligns well with previous studies (e.g., Ren et al., 2018, 2021; Schmölter & von Savigny, 2022; Schmölter et al., 2020a, 2020b; Vaishnav, Jacobi, Schmölter, & Dühnen, 2024; Vaishnav et al., 2019, 2022). The imbalance between the production and loss of plasma in the lower thermosphere and the F region causes the delay (Ren et al., 2018, 2019). Ionospheric delay varies spatially, seasonally, with altitude, and in response to changing solar activity conditions (Schmölter

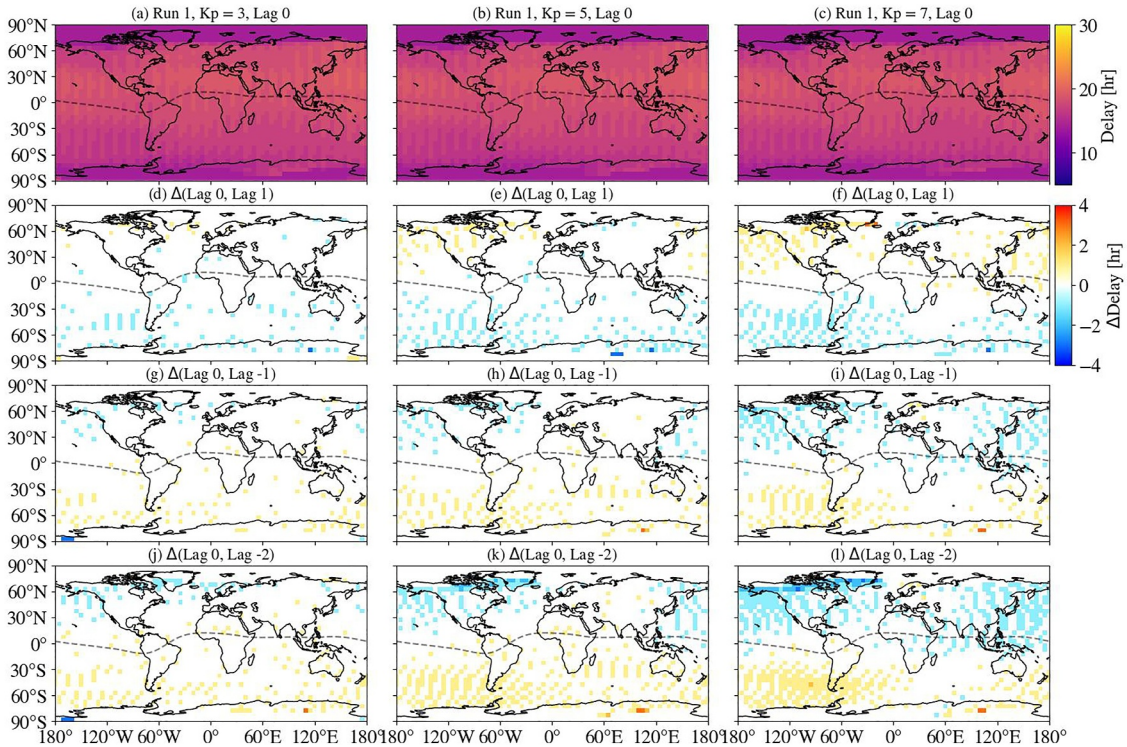

Figure 11. Same as Figure 10, but for Period 3.

et al., 2022, 2024; Vaishnav et al., 2019). This analysis extend prior research by highlighting the role of geomagnetic activity in the seasonal variation of the ionospheric delay (e.g., Schmölter et al., 2020a, 2020b; Vaishnav et al., 2022). It also systematically investigates the effects under different solar and geomagnetic activity conditions.

The mean ionospheric delay calculated during Period 2, based on the observed TEC and the F10.7 index, is approximately 24 hr. In contrast, during other periods, the mean delay is around 17 hr. This delay increases with solar activity, as noted in previous studies (Schmölter et al., 2024). Additionally, the variability of ionospheric delay observed across different latitudes is influenced by solar and geomagnetic activity conditions.

The TIE-GCM simulations show similar variations, although with slight differences in magnitude for the All Variability Run. When comparing it to the Solar Variability Run, the ionospheric delay during Period 2 increases by 3–6 hr in the Western Hemisphere, while it decreases by 1–3 hr in the Eastern Hemisphere. Compared to Period 2, there is a slight increase in ionospheric delay in the NH high-latitude region during Period 3, while delays decrease at other latitudes (see Figure 7). The comparison shows that geomagnetic activity significantly affects ionospheric composition, altering the delay. Simulation results indicate ionospheric delay varies with geomagnetic activity based on the season. The current results align with findings from previous studies (Schmölter et al., 2020b; Vaishnav, Schmölter, et al., 2021). For example, Schmölter et al. (2020b) identified seasonal and spatial variations in ionospheric delay, emphasizing the influence of geomagnetic activity. Additionally, Ren et al. (2018) reported the effects of changes in composition, specifically the O/N_2 ratio, on ionospheric delay. Several authors (Martinez & Lu, 2023; Qian et al., 2022; Vaishnav, Jacobi, Berdermann, et al., 2024) have investigated hemispheric differences in the O/N_2 ratio, which are affected by seasonal wind circulation patterns. Notably, Qian et al. (2022) found an asymmetric pattern between the hemispheres, which is associated with seasonal geomagnetic activity and variations in mean circulation (Martinez & Lu, 2023).

To assess the performance of the model for both the All Variability Run and the Solar Variability Run, we calculated the MAE values between the observed and modeled global ionospheric delays. The results indicate that during Period 2, which is dominated by solar activity, the MAE for the All Variability Run is approximately

4.4 hr, compared to 6.6 hr for the Solar Variability Run. In Period 3, when solar activity is lower than in Period 2, the MAE values are about 3 hr for the All Variability Run and 3.5 hr for the Solar Variability Run.

Furthermore, the MAE analysis demonstrates that in Period 2, the All Variability Run decreases the delay by about 2 hr compared to the Solar Variability Run. Specifically, the delays are 2.8 and 3.7 hr for the All Variability Run versus 5.3 and 5.9 hr for the Solar Variability Run in low- and mid-latitude regions. In Period 3, the All Variability Run reduces the delay by approximately 1 hr compared to the Solar Variability Run, with values of 1 and 2 hr for the All Variability Run and 2 and 3 hr for the Solar Variability Run in low- and mid-latitude regions. This suggests that during periods of higher solar activity, the MAE improves slightly compared to conditions of moderate solar activity.

Furthermore, the impact of geomagnetic activity on the delayed ionospheric response has also been investigated by considering different lag of geomagnetic activity. The simulation results show that ionospheric delay increases with higher geomagnetic activity levels (Kp = 3, 5, 7). Lagged effects of geomagnetic activity are evident in Periods 1 and 3, varying by day, season, and hemisphere, with delay differences of approximately 1–3 hr (see Figures 10 and 11, respectively).

Previously, Schmölter et al. (2020a) used TIE-GCM simulations to investigate the effect of solar and geomagnetic activity on the delayed response of the ionosphere. They reported an ionospheric delay of approximately 15 hr for a Kp-index of 0.91 and a delay of 17 hr for a Kp-index of 2.88 during December, indicating that geomagnetic activity influences this delay. Their study emphasized the significant role of transport processes in these delays. The current analysis, based on controlled simulations, shows a similar impact of geomagnetic activity on the delayed ionospheric response. The ionospheric delay generally increases with geomagnetic activity under moderate solar activity. However, during high solar activity, the effects of geomagnetic activity are less pronounced.

This study systematically assess the ability of the model to investigating the impact of geomagnetic activity on the delayed ionospheric response through controlled simulations. The results confirm previous findings and provide insight into the important role of geomagnetic activity in the delayed ionospheric response (Schmölter et al., 2020a, 2020b). In future investigations, considering the previous studies (Schmölter et al., 2024; Vaishnav, Jacobi, Schmölter, & Dühnen, 2024) and our new findings, we will examine the individual and combined effects of solar activity, geomagnetic storms, and lower atmospheric forcing for a thorough analysis.

The key findings from this study can be summarized as follows:

- The model simulation shows that the geomagnetic activity significantly alters the thermosphere-ionosphere composition, modifying ionospheric delay.
- Ionospheric delay varies with geomagnetic activity depending on season and solar activity.
- Increased solar activity leads to longer ionospheric delay.
- Lagged geomagnetic effects depend on season, geomagnetic activity, and solar activity.

Conflict of Interest

The authors declare no conflicts of interest relevant to this study.

Data Availability Statement

IGS TEC maps can be downloaded from https://cddis.nasa.gov/archive/gnss/products/ionex/ (NASA, 2025a). Daily Kp indices have been downloaded from https://omniweb.gsfc.nasa.gov/form/dx1.html (NASA, 2025b). The F10.7 index at 1 AU have been obtained from the LISIRD database (LASP, 2025, https://lasp.colorado.edu/lisird/). GUVI O/N_2 data are available at: http://guvitimed.jhuapl.edu/data/products (NASA, 2025c). The TIE-GCM simulation data used for this work can be accessed at https://doi.org/10.5281/zenodo.15313145 (Vaishnav, 2025).

Acknowledgments
The study has been supported by Deutsche Forschungsgemeinschaft (DFG, German Research Foundation) under project no. 495912049. Open Access funding enabled and organized by Projekt DEAL.

References

Blanc, M., & Richmond, A. (1980). The ionospheric disturbance dynamo. *Journal of Geophysical Research*, *85*(A4), 1669–1686. https://doi.org/10.1029/JA085iA04p01669

Burns, A., Killeen, T., Wang, W., & Roble, R. (2004). The solar-cycle-dependent response of the thermosphere to geomagnetic storms. *Journal of Atmospheric and Solar-Terrestrial Physics*, *66*(1), 1–14. https://doi.org/10.1016/j.jastp.2003.09.015

Cai, X., Burns, A. G., Wang, W., Qian, L., Solomon, S. C., Eastes, R. W., et al. (2021). Investigation of a neutral "Tongue" observed by GOLD during the geomagnetic storm on May 11, 2019. *Journal of Geophysical Research*, *126*(6), e2020JA028817. https://doi.org/10.1029/2020ja028817

Christensen, A. B., Paxton, L. J., Avery, S., Craven, J., Crowley, G., Humm, D. C., et al. (2003). Initial observations with the global ultraviolet imager (GUVI) in the NASA TIMED satellite mission. *Journal of Geophysical Research*, *108*(A12), 1451. https://doi.org/10.1029/2003ja009918

Codrescu, M., Fuller-Rowell, T., Foster, J., Holt, J., & Cariglia, S. (2000). Electric field variability associated with the millstone hill electric field model. *Journal of Geophysical Research*, *105*(A3), 5265–5273. https://doi.org/10.1029/1999JA900463

Codrescu, M. V., Codrescu, S. M., & Fedrizzi, M. (2022). Storm time neutral density assimilation in the thermosphere ionosphere with TIDA. *Journal of Space Weather and Space Climate*, *12*, 16. https://doi.org/10.1051/swsc/2022011

Dühnen, H., Vaishnav, R., Jacobi, C., Schmölter, E., & Berdermann, J. (2024). Comparative case study of delayed ionospheric response to a superposed 27-day solar rotation signal. *Advances in Space Research*. https://doi.org/10.1016/j.asr.2024.12.004

Fang, T.-W., Fuller-Rowell, T., Yudin, V., Matsuo, T., & Viereck, R. (2018). Quantifying the sources of ionosphere day-to-day variability. *Journal of Geophysical Research*, *123*(11), 9682–9696. https://doi.org/10.1029/2018JA025525

Fernandez-Gomez, I., Fedrizzi, M., Codrescu, M. V., Borries, C., Fillion, M., & Fuller-Rowell, T. J. (2019). On the difference between real-time and research simulations with CTIPe. *Advances in Space Research*, *64*(10), 2077–2087. https://doi.org/10.1016/j.asr.2019.02.028

Fong, W., Chu, X., Lu, X., Chen, C., Fuller-Rowell, T. J., Codrescu, M., & Richmond, A. D. (2015). Lidar and CTIPe model studies of the fast amplitude growth with altitude of the diurnal temperature "tides" in the Antarctic winter lower thermosphere and dependence on geomagnetic activity. *Geophysical Research Letters*, *42*(3), 697–704. https://doi.org/10.1002/2014gl062784

Fuller-Rowell, T., Codrescu, M., Moffett, R., & Quegan, S. (1994). Response of the thermosphere and ionosphere to geomagnetic storms. *Journal of Geophysical Research*, *99*(A3), 3893–3914. https://doi.org/10.1029/93JA02015

Günzkofer, F., Liu, H., Liu, H., Stober, G., Lu, G., Wu, H., et al. (2025). High-latitude joule heating in tie-gcm 3.0: Evaluation of different plasma convection forcing models. *Geophysical Research Letters*, *52*(17), e2025GL117647. https://doi.org/10.1029/2025GL117647

Günzkofer, F., Liu, H., Stober, G., Pokhotelov, D., & Borries, C. (2024). Evaluation of the empirical scaling factor of joule heating rates in TIE-GCM with EISCAT measurements. *Earth and Space Science*, *11*(4), e2023EA003447. https://doi.org/10.1029/2023EA003447

Heelis, R., Lowell, J. K., & Spiro, R. W. (1982). A model of the high-latitude ionospheric convection pattern. *Journal of Geophysical Research*, *87*(A8), 6339–6345. https://doi.org/10.1029/JA087iA08p06339

Hernández-Pajares, M., Juan, J. M., Sanz, J., Orus, R., Garcia-Rigo, A., Feltens, J., et al. (2009). The IGS VTEC maps: A reliable source of ionospheric information since 1998. *Journal of Geodesy*, *83*(3–4), 263–275. https://doi.org/10.1007/s00190-008-0266-1

Houminer, Z., & Soicher, H. (1994). Assessment of foF2 short-term variations from transionospheric time-delay measurements. In *Proceedings-international beacon satellite symposium edited by kersley, l* (pp. 136–140).

Jacobi, C., Jakowski, N., Schmidtke, G., & Woods, T. N. (2016). Delayed response of the global total electron content to solar EUV variations. *Advances in Radio Science*, *14*, 175–180. https://doi.org/10.5194/ars-14-175-2016

Jakowski, N., Fichtelmann, B., & Jungstand, A. (1991). Solar activity control of ionospheric and thermospheric processes. *Journal of Atmospheric and Terrestrial Physics*, *53*(11–12), 1125–1130. https://doi.org/10.1016/0021-9169(91)90061-b

Kouris, S. S., Xenos, T. D., Polimeris, K. V., & Stergiou, D. (2004). TEC and foF2 variations: Preliminary results. *Annals of Geophysics*, *47*(4), 6. https://doi.org/10.4401/ag-3346

Krankowski, A., Shagimuratov, I., & Baran, L. (2007). Mapping of foF2 over Europe based on GPS-derived TEC data. *Advances in Space Research*, *39*(5), 651–660. https://doi.org/10.1016/j.asr.2006.09.034

LASP. (2025). LASP interactive solar irradiance data center [Dataset]. *University of Colorado*. Retrieved from https://lasp.colorado.edu/lisird/

Martinez, B. C., & Lu, X. (2023). Quantifying day-to-day variability of O/N_2 and its correlation with geomagnetic activity using GOLD. *Frontiers in Astronomy and Space Sciences*, *10*, 1129279. https://doi.org/10.3389/fspas.2023.1129279

NASA. (2025a). GNSS atmospheric products [Dataset]. Retrieved from http://cddis.nasa.gov/Data_and_Derived_Products/GNSS/atmospheric_products.html

NASA. (2025b). Omniweb plus database [Dataset]. Retrieved from http://omniweb.gsfc.nasa.gov/

NASA. (2025c). TIMED GUVI observations [Dataset]. Retrieved from http://guvitimed.jhuapl.edu/data_products

Prölss, G. W. (2004). *Physics of the Earth's space environment*. Springer Berlin Heidelberg. https://doi.org/10.1007/978-3-642-97123-5

Qian, L., Burns, A. G., Emery, B. A., Foster, B., Lu, G., Maute, A., et al. (2014). The NCAR TIE-GCM: A community model of the coupled thermosphere/ionosphere system. In *Modeling the ionosphere–thermosphere system* (pp. 73–83). https://doi.org/10.1002/9781118704417.ch7

Qian, L., Gan, Q., Wang, W., Cai, X., Eastes, R., & Yue, J. (2022). Seasonal variation of thermospheric composition observed by NASA GOLD. *Journal of Geophysical Research*, *127*(6), e2022JA030496. https://doi.org/10.1029/2022ja030496

Qian, L., Wang, W., Burns, A. G., Chamberlin, P. C., & Solomon, S. C. (2020). Responses of the thermosphere and ionosphere system to concurrent solar flares and geomagnetic storms. *Journal of Geophysical Research*, *125*(3), e2019JA027431. https://doi.org/10.1029/2019JA027431

Ren, D., Lei, J., Wang, W., Burns, A., Luan, X., & Dou, X. (2018). Does the peak response of the ionospheric F2 region plasma lag the peak of 27-day solar flux variation by multiple days? *Journal of Geophysical Research*, *123*(9), 7906–7916. https://doi.org/10.1029/2018ja025835

Ren, D., Lei, J., Wang, W., Burns, A., Luan, X., & Dou, X. (2019). A simulation study on the time delay of daytime thermospheric temperature response to the 27-day solar EUV flux variation. *Journal of Geophysical Research*, *124*(11), 9184–9193. https://doi.org/10.1029/2019ja027000

Ren, D., Lei, J., Wang, W., Burns, A., Luan, X., & Dou, X. (2020). Different peak response time of daytime thermospheric neutral species to the 27-day solar EUV flux variations. *Journal of Geophysical Research*, *125*(7), e2020JA027840. https://doi.org/10.1029/2020ja027840

Richards, P. G., Fennelly, J. A., & Torr, D. G. (1994). EUVAC: A solar EUV flux model for aeronomic calculations. *Journal of Geophysical Research*, *99*(A5), 8981–8992. https://doi.org/10.1029/94ja00518

Richmond, A. D., & Maute, A. (2014). Ionospheric electrodynamics modeling. In *Modeling the ionosphere–thermosphere system* (pp. 57–71). https://doi.org/10.1002/9781118704417.ch6

Richmond, A. D., Ridley, E. C., & Roble, R. G. (1992). A thermosphere/ionosphere general circulation model with coupled electrodynamics. *Geophysical Research Letters*, *19*(6), 601–604. https://doi.org/10.1029/92gl00401

Rishbeth, H. (1998). How the thermospheric circulation affects the ionospheric F2 layer. *Journal of Atmospheric and Solar-Terrestrial Physics*, *60*(14), 1385–1402. https://doi.org/10.1016/s1364-6826(98)00062-5

Rishbeth, H., Sedgemore-Schulthess, K. J. F., & Ulich, T. (2000). Semiannual and annual variations in the height of the ionospheric F2-peak. *Annales Geophysicae*, *18*(3), 285–299. https://doi.org/10.1007/s00585-000-0285-6

Roble, R., & Ridley, E. (1987). An auroral model for the NCAR thermospheric general circulation model (TGCM). *Annales Geophysicae*, *5*, 369–382.

Schmölter, E., Berdermann, J., & Codrescu, M. (2021). The delayed ionospheric response to the 27-day solar rotation period analyzed with GOLD and IGS TEC data. *Journal of Geophysical Research*, *126*(2), e2020JA028861. https://doi.org/10.1029/2020ja028861

Schmölter, E., Berdermann, J., Jakowski, N., & Jacobi, C. (2020a). Modeling of the delayed ionospheric response with the TIE-GCM model. In *2020 European navigation conference (ENC)* (pp. 1–9). https://doi.org/10.23919/ENC48637.2020.9317355

Schmölter, E., Berdermann, J., Jakowski, N., & Jacobi, C. (2020b). Spatial and seasonal effects on the delayed ionospheric response to solar EUV changes. *Annales Geophysicae*, *38*(1), 149–162. https://doi.org/10.5194/angeo-38-149-2020

Schmölter, E., Berdermann, J., Jakowski, N., Jacobi, C., & Vaishnav, R. (2018). Delayed response of the ionosphere to solar EUV variability. *Advances in Radio Science*, *16*, 149–155. https://doi.org/10.5194/ars-16-149-2018

Schmölter, E., Dühnen, H., Berdermann, J., Vaishnav, R., & Jacobi, C. (2024). Spatial features of the delayed ionospheric response during low and high solar activity. *Journal of Geophysical Research*, *129*(5), e2024JA032672. https://doi.org/10.1029/2024JA032672

Schmölter, E., Heymann, F., Savigny, C., & Berdermann, J. (2022). The height-dependent delayed ionospheric response to solar EUV. *Journal of Geophysical Research*, *127*(3), e2021JA030118. https://doi.org/10.1029/2021ja030118

Schmölter, E., & von Savigny, C. (2022). Solar activity driven 27-day signatures in ionospheric electron and molecular oxygen densities. *Journal of Geophysical Research*, *127*(9), e2022JA030671. https://doi.org/10.1029/2022ja030671

Shim, J. S., Tsagouri, I., Goncharenko, L., Rastaetter, L., Kuznetsova, M., Bilitza, D., et al. (2018). Validation of ionospheric specifications during geomagnetic storms: TEC and foF2 during the 2013 March storm event. *Space Weather*, *16*(11), 1686–1701. https://doi.org/10.1029/2018SW002034

Strickland, D., Meier, R., Walterscheid, R., Craven, J., Christensen, A., Paxton, L., et al. (2004). Quiet-time seasonal behavior of the thermosphere seen in the far ultraviolet dayglow. *Journal of Geophysical Research*, *109*(A1), A01302. https://doi.org/10.1029/2003JA010220

Sutton, E., Forbes, J., & Knipp, D. (2009). Rapid response of the thermosphere to variations in Joule heating. *Journal of Geophysical Research*, *114*(A4). https://doi.org/10.1016/j.jastp.2004.03.026

Vaishnav, R. (2025). TIE-GCM simulations [Dataset]. *Zenodo*. https://doi.org/10.5281/zenodo.15313145

Vaishnav, R., Jacobi, C., & Berdermann, J. (2019). Long-term trends in the ionospheric response to solar extreme-ultraviolet variations. *Annales Geophysicae*, *37*(6), 1141–1159. https://doi.org/10.5194/angeo-37-1141-2019

Vaishnav, R., Jacobi, C., Berdermann, J., Codrescu, M., & Schmölter, E. (2021). Role of eddy diffusion in the delayed ionospheric response to solar flux changes. *Annales Geophysicae*, *39*(4), 641–655. https://doi.org/10.5194/angeo-39-641-2021

Vaishnav, R., Jacobi, C., Berdermann, J., Schmölter, E., & Codrescu, M. (2018). Ionospheric response to solar EUV variations: Preliminary results. *Advances in Radio Science*, *16*, 157–165. https://doi.org/10.5194/ars-16-157-2018

Vaishnav, R., Jacobi, C., Berdermann, J., Schmölter, E., & Codrescu, M. (2022). Delayed ionospheric response to solar extreme ultraviolet radiation variations: A modeling approach. *Advances in Space Research*, *69*(6), 2460–2476. https://doi.org/10.1016/j.asr.2021.12.041

Vaishnav, R., Jacobi, C., Berdermann, J., Schmölter, E., Dühnen, H., & Codrescu, M. (2024). Ionospheric response to solar EUV radiation variations using GOLD observations and the CTIPe model. *Journal of Geophysical Research*, *129*(1), e2022JA030887. https://doi.org/10.1029/2022JA030887

Vaishnav, R., Jacobi, C., Schmölter, E., & Dühnen, H. (2024). Influence of lower atmospheric variability: An investigation of delayed ionospheric response to solar activity. *Journal of Geophysical Research*, *129*(11), e2024JA032999. https://doi.org/10.1029/2024JA032999

Vaishnav, R., Schmölter, E., Jacobi, C., Berdermann, J., & Codrescu, M. (2021). Ionospheric response to solar extreme ultraviolet radiation variations: Comparison based on CTIPe model simulations and satellite measurements. *Annales Geophysicae*, *39*(2), 341–355. https://doi.org/10.5194/angeo-39-341-2021

Yao, Y., Liu, L., Kong, J., & Zhai, C. (2016). Analysis of the global ionospheric disturbances of the March 2015 great storm. *Journal of Geophysical Research: Space Physics*, *121*(12), 12157–12170. https://doi.org/10.1002/2016JA023352

Yu, T., Wang, W., Ren, Z., Cai, X., Liu, L., He, M., et al. (2022). Diagnostic analysis of the physical processes underlying the long-duration O/N_2 depletion during the recovery phase of the 8 June 2019 geomagnetic storm. *Journal of Geophysical Research: Space Physics*, *127*(12), e2022JA031075. https://doi.org/10.1029/2022JA031075

Yu, Y., Wan, W., Zhao, B., Chen, Y., Xiong, B., Liu, L., et al. (2013). Modeling the global NmF2 from the GNSS-derived TEC-GIMs. *Space Weather*, *11*(5), 272–283. https://doi.org/10.1002/swe.20052